Chapter 5

Fluorescence recovery after photobleaching experiments to study micro-scale mechanical properties

5.1 Introduction

The tunability of the mechanical properties of any polymer matrix is important for applications. Polyethylene glycol (PEG) is one such polymer that has wide-ranging applications from the field of drug delivery to 3D bio-printing for the production of nanomedicines and biodegradable scaffolds [1, 2, 3, 4, 5]. To achieve the desirable properties, certain fillers like clay, cellulose, and polyelectrolytes are incorporated into the polymer matrix [6, 7]. The applicability of these nanocomposites is dependent on specific characteristics/properties for specific applications. For example, in the case of drug delivery application, the nanocomposite is required to flow through viscoelastic media like extracellular matrix, phospholipid membranes, or blood plasma which require structural integrity for target-specific release mechanism [8, 9]. Therefore, it is important to complement the study of static mechanical properties at the macroscopic scale with a study of dynamic as well as static mechanical properties at the microscopic scale.

PEG molecules, when dissolved in water, have been found to make dynamic intra-molecular hydrogen bonding with the water molecules. These H-bonds act as a link between the neighboring chains thereby creating a bridge with the help of water molecules. These intermolecular associations have reversible kinetics. This association-dissociation kinetics of the PEG-water bonds can lead to

interesting dynamics within the polymer matrix where the segmental, as well as chain relaxation, can be observed [10]. The polymers with H-bonding have been found to possess heterogeneous dynamics which has been observed in neutron spin echo experiments [11]. Due to the presence of inter and intra-molecular associations, the polymer dynamics is also found to depart from the Rouse-like dynamics at a length scale higher than a few Kuhn lengths [11]. Macroscale experiments like frequency sweep and oscillatory shear experiments often reveal heterogeneous dynamics. For concentrated solutions and melts of associated polymers, these experiments have revealed the presence of fast segmental dynamics with a scaling exponent higher than the Rouse scaling (0.5) [12]. Several theoretical models, like sticky reptation models, or sticky Rouse models have been developed to explain the mechanical response by incorporating a reversible network formation in the Rouse and reptation models [13, 14, 15, 16, 17, 18]. Simulations have also been popular in determining the effect of these associating systems on the static and dynamic mechanical properties but the limitation of size in simulations makes it less reliable [19, 20, 21]. Hence, it is evident from past experiments and simulations that the associating polymers have complicated dynamics. The introduction of nanoparticles in the system could lead to further complications of the diffusion dynamics. Therefore, for the development PEG based nanocomposites with tunable mechanical properties, it is important to study the micro-scale diffusion dynamics of the system.

Another important aspect is that the incorporation of nanoparticles like clay may lead to additional interactions like depletion interactions and some associative interactions between the polymer and clay particles. These interactions are concentration-dependent and can produce micro-scale to macro-scale phase separations in the nanocomposites. The phase boundaries then lead to the development of stresses, which, in turn, affect the mechanical response of the overall material. These heterogeneities make the system more susceptible to cavity and crack formation and fractures [22]. Therefore, determining the optimal concentration of the polymer and nanoparticle is a must for the development of materials with targeted mechanical properties [23, 24, 25, 26, 27, 28]. The possible development of heterogeneities implies that simply tuning the concentration of polymer and nanoparticles cannot give an optimized and customized mechanical response. Several other characteristics

which can hinder the formation of desired polymer nanocomposites include, yielding, gelation, aging, flow-induced shear banding, and micro-structuring [23, 28, 29, 30, 31]. Therefore, a simultaneous measurement of micro-structure is a must along with the diffusion dynamics. Several studies have proved that the microstructures affect the mechanical response with the help of scattering experiments [27, 28, 32, 33]. Several experimental, theoretical, and simulation studies on nanoparticle-reinforced polymer matrices have revealed a varying degree of mechanical modification of the host polymer matrix by nanoparticles as a result of additional length and time scales introduced due to interactions [20, 34, 35, 36, 37, 38, 39, 40].

In this chapter, we have aimed to address the above factors experimentally by studying the overall structure and dynamics of the PEG matrix by incorporating two types of nanoparticles: bentonite (clay nanoparticles) and carboxymethyl cellulose (CMC) nanofibers. This chapter explores the effect of associative intermolecular interactions between polymer chains and phase separation due to depletion interactions in presence of colloidal clay particles, on micro-scale dynamics. The fluorescence recovery after photobleaching (FRAP) technique has been used to measure diffusion coefficients. The FRAP experiments reveal the diffusion dynamics to be very sensitive to the phase separations induced by depletion interactions at the micro-scale. A method to analyze static solution microstructure is presented by calculation of structure factor from fluorescence microscopy images. SAXS and MSANS and phase contrast microscopy experiments are also conducted to analyze the solution microstructure at different length scales in the presence and absence of nanoparticles. An interrelation between the solution microstructure and the diffusion at the micro-scale of a fluorescent probe is presented. In this chapter, we also analyze the applicability of fluorescence recovery after photobleaching (FRAP) technique for the determination of the mechanical response of the solutions at the micro-scale.

5.2 Preparation of polymer solutions

Polyethylene glycol (PEG) of molecular weight 20,000M was purchased from Alfa Aesar and used without further processing. Aqueous solutions of PEG were prepared by dissolving the appropriate amount of PEG in deionized water

(Loba chemicals) to make 5, 10, 20, and 50 percent by weight solution concentration. The solutions were prepared by stirring the mixture with a magnetic stirrer for one hour at room temperature, around 30 °C. For the fluorescence microscopy experiments, fluorescein disodium salt (Alfa Aesar) was added to get a concentration of 30 μM fluorescein in the PEG solution. Solutions of PEG having 0.01, 0.1, and 1 wt.% of nanoclay bentonite (Sigma) and carboxy methyl cellulose (sodium salt, 90,000M molecular weight, the degree of substitution = 0.7 carboxymethyl groups per anhydroglucose unit, from Sigma) were prepared following the procedure mentioned above. The clay samples were aged for 1 day before the experiments to maintain uniform aging for all the clay samples.

5.3 Fluoresecence recovery after photobleaching (FRAP)

Fluorescence recovery after photobleaching (FRAP) is a versatile technique that is used to measure the transport mechanism and molecular diffusion. This technique involves photobleaching of fluorescent species and studying the diffusion of unbleached species into the photobleached region. It was developed in 1970 to investigate the diffusion of proteins in membranes. Since its development, FRAP has been used in a wide range of applications from the investigation of transport and kinetics in living cells and tissues to the study of diffusion phenomenon that contributes to the properties of products in various food, textile, cosmetic, and pharmaceutical industry [41]. Over few years this technique is also being used to study the diffusion in complex heterogeneous structures like colloids, gels, and other biomaterials to study the diffusion process at the local level [42]. Another important technique that is used to study molecular diffusion is fluorescence correlation spectroscopy (FCS) which measures the intensity fluctuations in a specimen to determine the diffusion dynamics. FCS is a highly sensitive tool that is influenced by the variable concentration of a specimen and it has high spatial and temporal resolution [43]. However, both FRAP and FCS can accurately probe the diffusion within the sample but FCS is not able to measure the heterogeneities in the diffusion which can be measured using FRAP [44]. Another drawback of FCS is also that it is not

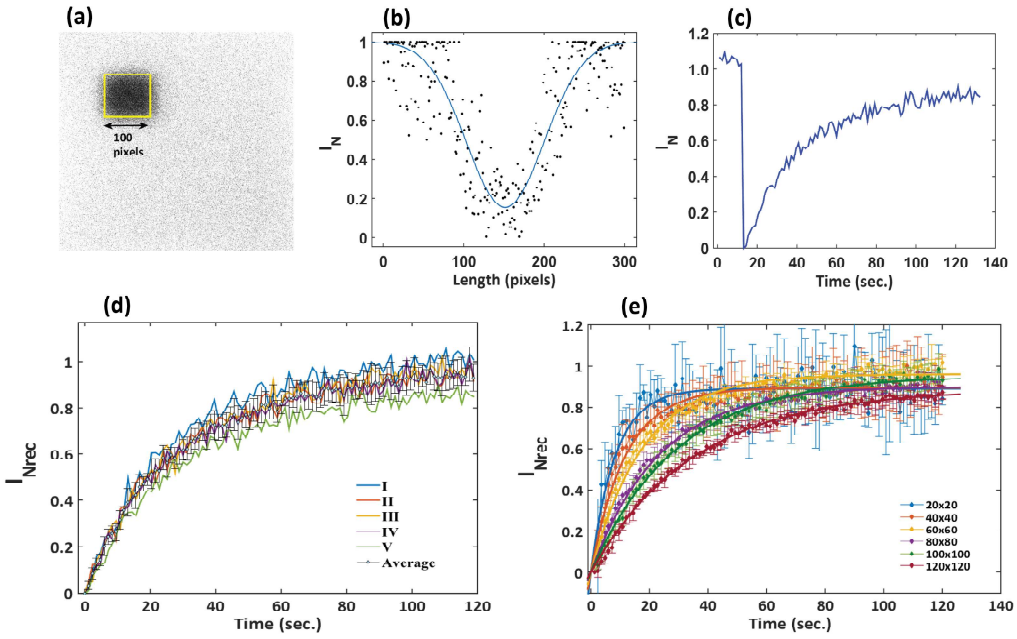

FIGURE 5.1: (a) 100x100 pixel area photobleached during FRAP experiments for PEG solution. (b) Normalized fluorescence intensity profile with a spotwidth fitted to Gaussian function (Equation 5.1). (c) Normalized mean intensity curve for 50 wt.% PEG. (d) Normalized recovery curves for 5 individual photobleached regions and its mean recovery profile for 50 wt.% PEG. (e) Normalized recovery curves of 50 wt.% PEG for different sizes of photobleached region.

able to measure the immobile fraction within the sample and also it is not suitable for the sample which has aggregates that can be measured using FRAP [43]. Therefore, we have developed a methodology using FRAP to study the micro-scale mechanical properties via diffusion of fluorescent probes in polymer solutions and polymer nanocomposite solutions.

5.3.1 Instrumental setup

A confocal laser scanning microscope was used to perform FRAP experiments at the Center for Cellular and Molecular Platforms (C-CAMP) facility at National Center for Biological Sciences (NCBS), Bangalore. The setup included an Olympus IX83 Fluo View FV3000 confocal laser scanning microscope (CLSM) with 60x/1.35 numerical aperture UPLAN APO oil immersion Olympus

objective. The XY scanning mode of the microscope was used with a spatial resolution of 0.414 μm per pixel and a time resolution of 1.2 sec. An excitation wavelength of 488nm was used from OBIS coherent laser source. All the experiments were conducted at room temperature which was maintained at 22 °C.

5.3.2 Diffusion analysis using FRAP

To perform FRAP experiments rectangular images of 512x512 pixels were captured and a rectangular region of interest (ROI) of dimension 100x100 pixels was chosen for photobleaching as shown in Figure 5.1(a). The ROI was photobleached with 100% laser power for 2 secs. and the rest of the images were captured between 1-3% laser power. About 10 images were captured before photobleaching and 90 images were captured after photobleaching. The experiment was repeated for 5 different regions in the same sample and the resultant of the five observations was calculated and analyzed further using custom-made programs in MATLAB.

A 512-pixel line intensity profile was extracted from the center of the photobleached region of the first image obtained after photobleaching and was fitted to a Gaussian function (Equation 5.1) to determine the spotwidth r_e of the bleached region [45]. The Gaussian fit (Equation 5.1) is shown in Figure 5.1(b) and the spot width was calculated to be 91.3 $\pm$ 5 pixels or 37.82 $\pm$ 2 μm.

$$f(x) = 1 - k\exp(\frac{-2(x-c)^2}{r_e^2}) \tag{5.1}$$

The FRAP images were normalized and corrected from the background and photofading. These corrections and normalization were performed using the following equation[46, 47]:

$$I(t) = \frac{I_{data} - I_0}{I_{whole} - I_0} \tag{5.2}$$

In the above Equation (5.1), I_{data} is the mean intensity of the photobleached region, I_0 is the mean intensity of the photobleached region immediately after photobleaching, and I_{whole} is the mean intensity of the entire frame. After this, the normalized recovery profiles were obtained as shown in Figure 5.1(c) and were investigated for calculation of diffusion coefficient (D). Since 5 different sets

were obtained for each sample, a mean intensity profile was calculated for each with standard deviation which was used for further analysis. The recovery curve for 5 different regions and its mean recovery curve for 50 wt.% PEG solution is shown in Figure 5.1(d). The size of the bleached region was optimized by varying the photobleaching region by 50 wt.% PEG for 20x20, 40x40, 60x60, 100x100, and 120x120 pixels, the recovery profiles for the same are given in Figure 5.1(e). Since the size of the nanoparticles can be up to a few μm so 100x100 or 120x120 pixels can be considered as an ideal size.

To calculate the diffusion coefficient (D), three different methods were employed. In the first and second methods, the normalized recovery profiles were fitted with an exponential function given by:

$$I_N(t) = I_\infty(1 - \exp(-t/\tau)) \tag{5.3}$$

here, $I_N(t)$ is the normalized intensity, τ is the diffusion time and I_∞ is the postbleach saturation intensity. The recovery after photobleaching is unable to reach the prebleach value because of the presence of immobile constituents in the solution. The immobile fraction can, therefore, be calculated as the difference between the recovery curve and the prebleach curve as $1 - I_\infty$. From $I_N(t)$, the half recovery time ($t_{1/2}$) is calculated which is the point where the recovery is $0.5I_\infty$. For the known value of $t_{1/2}$, D can therefore be calculated as [45, 48]:

$$D = \frac{0.224 r_n^2}{t_{1/2}} \tag{5.4}$$

and,

$$D = \frac{r_n^2 + r_e^2}{t_{1/2}} \tag{5.5}$$

In the above equations, r_n is the actual radius of the photobleached region (50 pixels, or 20.7 μm) and r_e is the effective radius or spotwidth of the photobleached region (91.35 pixels or 37.82 μm), which was calculated by fitting the postbleach recovery profile to a Gaussian (Equation 5.1).

For the third method of determining D, the normalized postbleach recovery profiles were fitted to [49]:

$$I_N(t) = I_\infty(1 - \sqrt{w^2(w^2 + 4\pi D t)^{-1}}) \tag{5.6}$$

where $I_N(t)$ is the mean normalized time dependent post bleach recovery fluorescence intensity, I_∞ is the asymptotic fluorescence intensity, w is the half-width of the bleached ROI (20.7 μm) and D is the diffusion coefficient. The D values obtained from Equations 5.4, 5.5, and 5.6 for fluorescein in water were compared to the D value obtained from the Stoke-Einstein relation to check the reliability of the methods.

5.4 Micro-scale mechanical properties from diffusion

Fluorescence recovery after photobleaching (FRAP) experiments are performed to study the diffusion of fluorescent probes in the polymer solution and polymer nanocomposite solution. Diffusion is a phenomenon that gives insight into the micro-scale mechanical properties of the material. Since the diffusion phenomenon is sensitive to the inhomogeneities present in the material, therefore, it is dependent on the size of the fluorescent particle (R) and the size/correlation length (ξ) of the network formed by overlapping polymer chains [50, 51, 52, 53]. Depending upon the size of the fluorescent particle and polymer chain, the diffusion phenomenon can be studied in three different regimes:

1. When the ratio of fluorescent particle size to the correlation length of the polymer is less than 1,
$$\frac{R}{\xi} << 1 \tag{5.7}$$
in this case, the overall diffusion of the particle can be governed by the solvent viscosity and the fluorescent probes are free to navigate through the polymer matrix.

2. When the ratio of fluorescent particle size to the correlation length of the polymer is greater than 1,
$$\frac{R}{\xi} >> 1 \tag{5.8}$$
here, the diffusion is governed by macroscopic viscosity which can be studied with the help of a rheometer.

3. When the ratio of fluorescent particle size to the correlation length of the polymer is in the intermediate regime,

$$\frac{R}{\xi} \approx 1 \tag{5.9}$$

in such a case, the diffusion is governed by the local viscosity of the polymer. The intermediate regime is important to study the micro-scale mechanical properties and heterogeneities in the material.

To study the micro-scale mechanical properties via diffusion, the intermediate regime is focused. Therefore, the ratio of the size of fluorescein (which is the fluorescent particle of interest) to the correlation length of PEG (polymer of interest) is chosen such that they fall in the intermediate regime. Five different concentrations of PEG are studied which is given in Table 5.1 along with their theoretical, experimental, and calculated correlation lengths and their ratio with the size of the fluorescent particle.

The weight percentages of the polymer solutions are converted into their volume fractions using the following formula:

$$c = \frac{\frac{c_{pol}}{\rho_{pol}}}{\frac{c_{pol}}{\rho_{pol}} + \frac{(100 - c_{pol})}{\rho_{sol}}} \tag{5.10}$$

where, c_{pol} is the concentration of polymer in weight percentage, ρ_{pol} is the density of the polymer, and ρ_{sol} is the density of solvent (water in our case). The correlation length for various concentrations of PEG is calculated from the overlap concentration in volume fraction of the polymer solution which can be represented as:

$$c* = \frac{M_w}{\frac{4}{3}\rho\pi R_g^3 N_A} \tag{5.11}$$

The overlap concentration of PEG solution from the above formula is calculated as 0.0289g/ml $\approx$ 0.03 g/ml. The theoretical value of R_g, in this case, is calculated from $R_g = 0.02 M_w^{0.58}$ = 6.246 nm and the experimental value of R_g was taken as 4.3 nm [54].

The volume fractions of all the concentrations of PEG (from 5 wt.% to 50 wt.%) are given in Table 5.1. It can be observed that the chosen range of

TABLE 5.1: Length scales (blob size ξ) and interaction strength (ϕ_{Dep}, depletion interactions in presence of bentonite) for different concentrations of PEG aqueous solutions.

Sample	Volume Fraction (c)	ξ_T (nm)	ξ_E (nm)	ξ_C (nm)	$\frac{R}{\xi_E}$	$\frac{R}{R_g}$	$\frac{b}{R_g}$	$\frac{\phi_{Dep}}{k_BT} = -\frac{3b}{2R_g}c = -8.7x10^{-3}c$
5P	0.042	4.6	3.3	11.5	0.15	0.116	5.8 X 10^3	0.35
10P	0.085	2.7	2.8	6.6	0.18			0.74
20P	0.18	1.56	1.12	3.86	0.45			1.53
30P	0.26	1.13	0.82	2.78	0.61			2.3
50P	0.456	0.75	0.54	1.8	0.93			3.9

concentrations is varying from semi-dilute to highly concentrated regime of the polymer solution. Once the volume fraction and the overlap concentration are known, the correlation length of the overlapping polymer chains (ξ) or the blob size can be determined as:

$$\xi = R_g(\frac{c}{c*})^{-0.76} \tag{5.12}$$

The ξ_E was also compared with the theoretical (ξ_T) and calculated (ξ_C) value which can be determined as:

$$\xi_c = c^{(\frac{-\nu}{3\nu-1})} \tag{5.13}$$

where, c is the volume fraction and the exponent ν = 0.588 for a neutral polymer in a good solvent. From Table 5.1, it can be seen that the correlation length of the polymer chain or the blob size ξ is varying between 0.5 to 3.5 nm. Accordingly, the ratio of the size of the fluorescent probe to the blob size of the polymer chain ($\frac{R}{\xi_E}$ as shown in Table 5.1) is close to 1 for some concentrations, which shows that the diffusion experiments are performed in the intermediate regime and it can provide insight about the micro-scale mechanical properties.

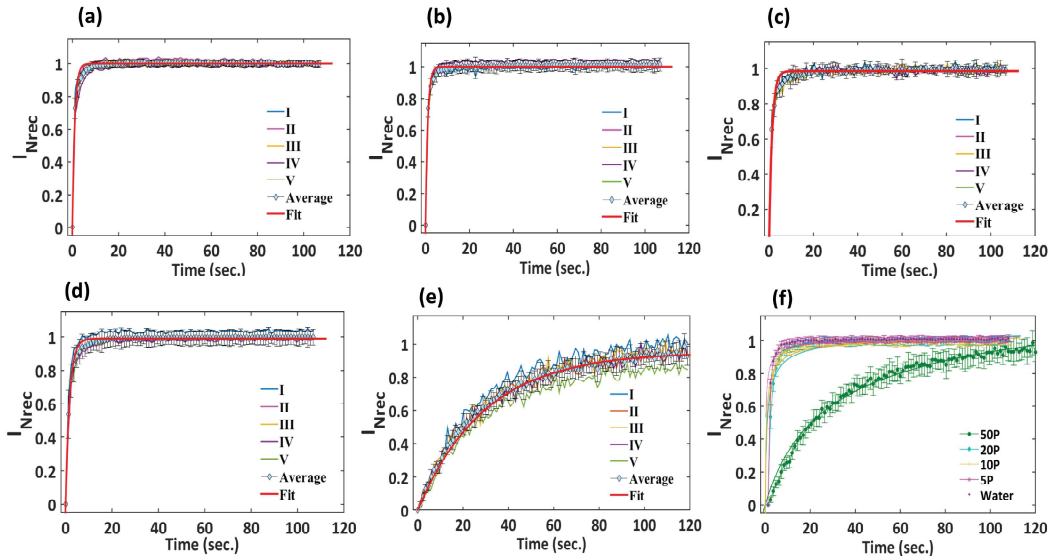

FIGURE 5.2: Normalized recovery profiles for (a) Control (only water), (b) 5P, (c) 10P, (d) 20P and (e)50P for 5 different regions and their mean normalized intensity with a fitting to Equation 5.3. (f) Fits of average recovery curves to Equation 5.6, for solutions of different PEG concentrations as mentioned in the legend.

TABLE 5.2: Diffusion coefficients as calculated from three different techniques: Equation 5.4 (D1), Equation 5.5 (D2) and Equation 5.6 (D3)

Sample	PEG (wt.%)	Bentonite (wt.%)	CMC (wt.%)	τ (sec)	$t_{1/2}$ (sec.)	M_{If}	D1 ($\mu m^2 sec^{-1}$)	D2 ($\mu m^2 sec^{-1}$)	D3 ($\mu m^2 sec^{-1}$)
Water	0	0	0	1.02 ± 0.04	0.70 ± 0.03	0	135 ± 6	401 ± 61	327 ± 15
5P	5	0	0	0.99 ± 0.04	0.68 ± 0.03	0	139 ± 6	544 ± 97	337 ± 16
10P	10	0	0	1.24 ± 0.07	0.85 ± 0.05	0.018 ± 0.005	111 ± 6	241 ± 29	270 ± 16
20P	20	0	0	1.736 ± 0.009	1.20 ± 0.06	0.01 ± 0.003	79 ± 4	143 ± 22	193 ± 10
50P	50	0	0	27.8 ± 0.7	19.2 ± 0.5	0.055 ± 0.007	4.9 ± 0.1	2.3 ± 0.1	12 ± 0.3
20P + 0.01B	20	0.01	0	17.5 ± 2.5	12.1 ± 1.7	0.361 ± 0.003	7.9 ± 1.1	6.9 ± 1.5	19.1 ± 2.7
20P + 0.1B	20	0.1	0	11.1 ± 0.1	7.7 ± 0.1	0.135 ± 0.002	12.3 ± 0.1	10 ± 1	29.9 ± 0.4
20 + 1B	20	1	0	5.7 ± 0.2	4 ± 0.15	0.067 ± 0.003	23.9 ± 0.8	33 ± 4	57 ± 2
0.01B	0	0.01	0	3.8 ± 0.1	2.6 ± 0.1	0.234 ± 0.004	35 ± 1	39 ± 6	87 ± 4
0.1B	0	0.1	0	3.3 ± 0.1	2.3 ± 0.1	0.25 ± 0.004	40 ± 2	49 ± 7	98 ± 5
1B	0	1	0	4.2 ± 0.3	2.9 ± 0.2	0.035 ± 0.003	33 ± 2	48 ± 5	81 ± 5
20P + 0.01C	20	0	0.01	1.7 ± 0.04	1.18 ± 0.03	0.03 ± 0.004	81 ± 2	111 ± 13	196 ± 5
20P + 0.1C	20	0	0.1	2.06 ± 0.05	1.42 ± 0.04	0.035 ± 0.004	67 ± 1	74 ± 9	162 ± 4
20P + 1C	20	0	1	2.06 ± 0.06	1.42 ± 0.04	0.049 ± 0.004	67 ± 2	81 ± 9	162 ± 5
0.01C	0	0	0.01	2.8 ± 0.1	1.9 ± 0.1	0.197 ± 0.003	48 ± 2	88 ± 10	117 ± 6
0.1C	0	0	0.1	2.4 ± 0.1	1.7 ± 0.08	0.187 ± 0.005	56 ± 2	77 ± 7	135 ± 6
1C	0	0	1	3 ± 0.1	2.1 ± 0.1	0.237 ± 0.03	44 ± 2	71 ± 12	108 ± 5

5.4.1 Diffusion of fluorescent probe in PEG solution

To study the effect of polymer concentration on the diffusion of fluorescent particles, different concentrations of PEG are selected as given in Table 5.2 and a control experiment of fluorescein particles in water is performed and the diffusion coefficients were calculated from the respective methods as illustrated in section 5.3. The normalized recovery profile for control experiments is shown in Figure 5.2(a) and the D values are given in Table 5.2. The D values for control experiments are compared to the Stokes-Einstein D value of fluorescein in water (with $\approx$ 0.5 nm as the hydrodynamic radius of fluorescein in water [55]), which is calculated as 386.2 $\mu m^2 sec^{-1}$ in the present experimental conditions. The D value obtained from Equation 5.6 matches this theoretical D value best (Table 5.1). The normalized recovery profile for the 5P solution is shown in Figure 5.2(b), where a fast diffusion is observed with minimum error in the five sets observed and negligible immobile fraction. Similar is the case with 10P (Figure 5.2(c)) with a fast recovery and minimum immobile fractions in the solution. On increasing the PEG concentration further to 20P, the recovery became slower with a larger error in the mean recovery (Figure 5.2(d)). This is a signature of the aggregates of polymer chains present in 20P. The 50P concentration shows maximum inhomogeneity in the recovery profile for five sets with the highest error and slowest recovery among all PEG concentrations observed as shown in Figure 5.2(e). This signifies that the polymer solution has entered a concentrated regime from the semi-dilute regime where micro-scale inhomogeneities are present.

The recovery curves for all concentrations are fitted with Equation 5.3 which is shown in red in Figure 5.2(a)-(e). The recovery curves are also fitted with Equation 5.5 to calculate D2 which is shown in Figure 5.2(f) for all the concentrations of PEG. The diffusion coefficient (D), diffusion time (τ), half recovery time ($t_{1/2}$) and the immobile fraction (M_{If}) for all the concentrations are given in Table 5.2. With increasing concentrations of PEG, the diffusion time is increasing, and therefore, the D values were decreasing indicating that for a higher concentration of polymer, the diffusion is slower and the solution is becoming more viscous.

As stated before, the diffusion phenomenon is dependent on the size of particles, but when a polymer is transformed into a polymer nanocomposite,

then the diffusion of fluorescent probes into the polymer nanocomposite matrix is also governed by the size and structure of the nanoparticle. When a nanofiller is incorporated into a polymer matrix, the distribution of the nanofiller is dependent on various enthalpic and entropic interactions between the polymer and nanoparticles. The ratio of the size of the nanoparticle to the polymer chain radius of gyration decides the whether the nanoparticle will form strings, sheets or spherical agglomerates [53] which has also been observed using theoretical models, experiments, and simulations in a polymer-clay nanocomposite [56]. Therefore it is interesting to study the diffusion of fluorescent probes in a polymer nanocomposite, where the diffusion of fluorophores is hindered by both the polymer and the nanoparticles present. For this purpose, two nanofillers of different structures are chosen: nanoclay bentonite which has a layered structure, and carboxymethyl cellulose (CMC) nanofibers to study the effect of nanofiller concentration on the diffusion and the micro-scale mechanical properties of the polymer nanocomposite. The nanofillers were introduced in 20P because its length scale is closest to the intermediate regime which can provide information about the micro-scale mechanical properties.

5.4.2 Effect of CMC nanofibers on diffusion

On addition of CMC nanofibers in 20P, the diffusion is similar to that observed in 20P with a very less scatter in the average recovery profiles. The average normalized recovery profiles for all three concentrations of CMC (0.01%C, 0.1%C, and 1%C) in 20P along with 20P are shown in Figure 5.3(a) and (b) and the average normalized recovery profiles for the control experiments with three concentrations of CMC (0.01%C, 0.1%C, and 1%C) in water are given in Figure 5.3 (c) and (d). From Figure 5.3 (a) it can be seen that the recovery profile for all concentrations of CMC in 20P resembles the same as 20P with a very fast diffusion and very less error bars indicating very less immobile fraction. But on comparing the recovery profile quantitatively, it is found that the immobile fraction was higher for CMC blends as compared to 20P which is stated in Table 5.2. This can be possibly due to the presence of aggregates in PEG+CMC solutions or it can also be due to the hindrance to the fluorescein diffusion by the presence of semi-flexible CMC chains. On comparing Figure 5.3 (a) and (b) it is observed that Equation 5.3 is a better fit to these recovery curves as compared to

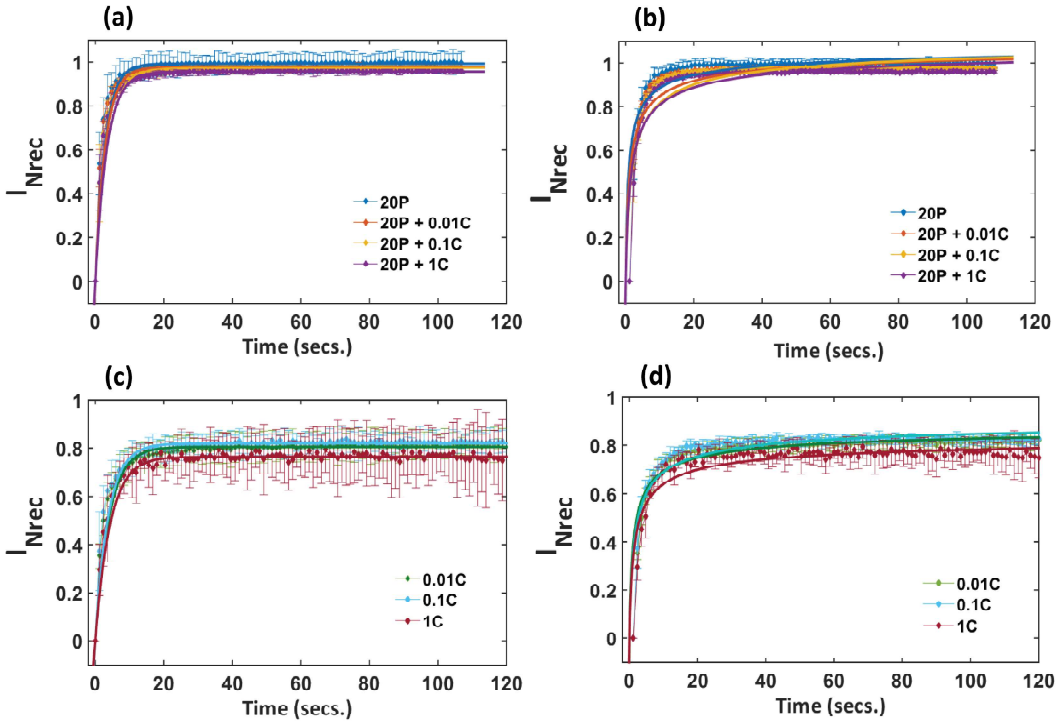

FIGURE 5.3: Normalized recovery profiles on adding CMC nanofibers to 20P for 0.01%C, 0.1%C and 1%C in 20P along with 20P and their respective fits to Equation 5.3 in (a) and Equation 5.6 in (b). The control experiments for 0.01%C, 0.1%C and 1%C in water and their respective fits to Equation 5.3 in (c) and Equation 5.6 in (d).

the Equation 5.6. Also, for only CMC solutions, Equation 5.3 is a better fit which is evident from comparing Figure 5.3(c) and (d).

The control experiments for aqueous solutions of CMC show higher amount of immobile fractions (Figure 5.3(c) and (d) and Table 5.2) as compared to PEG+CMC solutions which indicate higher inhomogeneity and immobile fractions in CMC solutions. This again points towards two possibilities, either the presence of CMC aggregates or the topological hindrance to fluorescein diffusion by semi-flexible CMC. A SANS study by Lopez et.al on the NaCMC solutions with concentrations ranging from unentangled semi-dilute to entangled concentrated regime showed the presence of weak aggregate formation of CMC which was evident from the scattering profile [57]. Another study with colloidal solutions of NaCMC in water has revealed network formation and aggregation of CMC which was dependent on the degree of substitution of the CMC particles [50]. Therefore, it can be inferred that the higher immobile fraction in the recovery curves on addition of CMC is due to the aggregation of CMC particles which is higher in the absence of polymer.

5.4.3 Effect of bentonite nanoparticles on diffusion

The normalized recovery profiles on adding bentonite nanoparticles to 20P are shown in Figure 5.4 (a) and (b) for all the three concentrations of bentonite,i.e., 0.01% (20P + 0.01B), 0.1% (20P + 0.1B) and 1% (20P + 1B) along with the 20P recovery profiles. It was observed that on adding bentonite nanoparticles, the scatter in the five sets of observations increased which is reflected in the form of high errorbars in Figure 5.4(a). The error in PEG + bentonite nanocomposites increased to about 30% greater than the initial 20P. The recovery in the PEG + bentonite nanocomposite was slower than in the 20P solution. For 20P+0.01B, the recovery experienced a larger $t_{1/2}$ but the scatter was lesser as compared to the higher concentrations (Figure 5.4(a)). For 20P + 0.1B, (Figure 5.4(a)) and 20P + 1B (Figure 5.4(c)), there is a huge scatter higher than 20P and 20P+0.01B, which leads to variable immobile fractions and large errorbars in their average recovery profiles. Also, on comparing Figure 5.4 (a) and (b) it was observed that Equation 5.3 was a better fit to these recovery curves as compared to Equation 5.6.

The D values on the addition of bentonite nanoparticles are given in Table 5.2. The $t_{1/2}$ values decreased and the D values increased with increasing bentonite

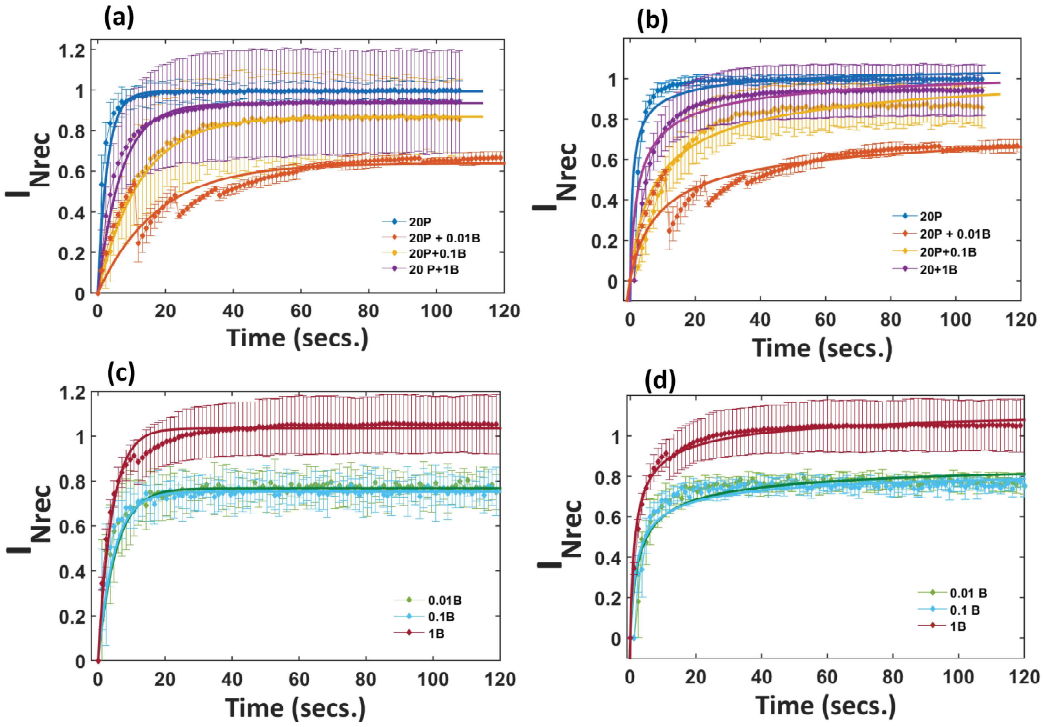

FIGURE 5.4: Normalized recovery profiles on adding bentonite to 20P for 0.01%B, 0.1%B and 1%B in 20P along with 20P and their respective fits to Equation 5.3 in (a) and Equation 5.6 in (b). The control experiments for 0.01%B, 0.1%B and 1%B in water and their respective fits to Equation 5.3 in (c) and Equation 5.6 in (d).

concentration, indicating a faster diffusion in higher bentonite concentration. The higher scatter in PEG+B solutions indicated the presence of heterogeneity in the microchannel. The $t_{1/2}$ and immobile fraction (M_{If}) values for different regions in PEG+B solutions are given in Table 5.3 which shows a remarkable presence of heterogeneity, especially in 20P+0.1B and 20P+1B. Recent computer simulations on spherical nanoparticles have shown that when the system becomes viscous the nanoparticles stick to the surface of the polymer and start moving along with the polymer chain which results in the slowing down of the polymer dynamics [58]. Therefore, the slow diffusion on increasing the concentration of bentonite can also be due to the increasing interactions between PEG and bentonite which can form aggregates.

Control experiments with only bentonite in solution are shown in Figure 5.4(c) and (d) respectively with two different fits. It is observed that only bentonite solutions showed faster diffusion (small τ) compared to the PEG + B systems but the inhomogeneity is persistent which is reflected in the form of high errorbars in the recovery curves of only bentonite solutions with the highest amount of inhomogeneities in 1B solution. The D values for only bentonite solutions are given in Table 5.2. Therefore, it can be established that the bentonite nanoparticles are undergoing aggregation which needed to be confirmed with further experiments.

5.4.4 Cluster analysis of diffusion coefficient

From an overall cluster analysis of diffusion half-time $t_{1/2}$, it is observed that the control experiment with water clusters together with 5P and 10P. 20P has a slightly higher $t_{1/2}$ than its lower concentrations therefore, it clusters with 20P+CMC (all concentrations) (Figure 5.5(a), red cluster). The addition of bentonite nanoparticles in PEG (PEG+B) forms three different clusters for three different concentrations of bentonite in PEG indicated by black, pink, and green clusters in Figure 5.5(a) implying the presence of aggregates and underlying the need for further study. 50P being the most viscous forms a separate cluster in cyan color (Figure 5.5(a)) and the control experiments of aqueous solutions of bentonite and CMC are clustered together (Figure 5.5(a), blue cluster). On comparison of the three D values calculated from different approaches it was observed that there was huge inconsistency in all the three theoretical values of

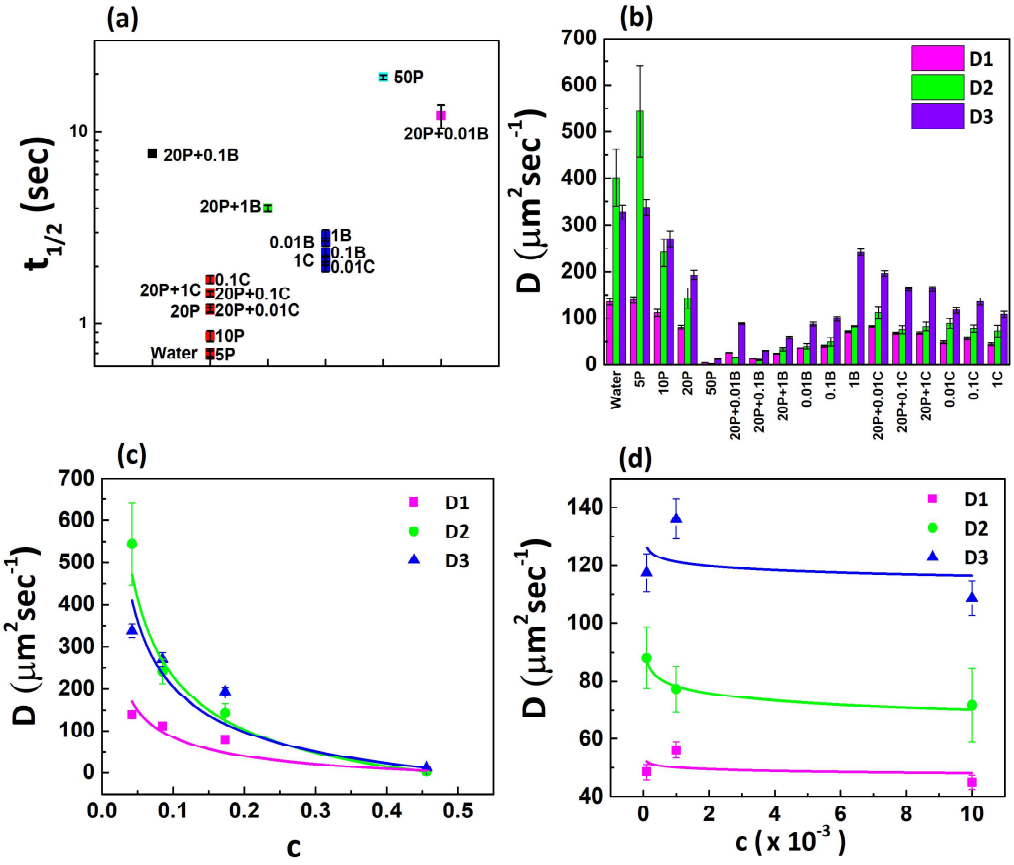

FIGURE 5.5: (a) Cluster graph of diffusion half time ($t_{1/2}$) for fluorescein in different solutions indicated with different colors. (b) Comparison of D values calculated from 3 different methods. (c) D values for different concentrations of PEG (pink) represented by a non-entangled Rouse scaling $D \sim c^{-0.54}$ (d) D values for CMC aqueous solutions with a scaling $D \sim c^0$, indicating D for CMC is independent of c.

TABLE 5.3: Heterogeneities and immobile fractions present in PEG+B solutions for all concentrations of bentonite in 20P

Sample	I_∞	τ (sec.)	$t_{1/2}$ (sec.)	$M_I f$
20P + 0.01B				
1	0.61 ± 0.01	12 ± 2	8 ± 1	0.3867 ± 0.01
2	0.64 ± 0.01	17 ± 2	12 ± 2	0.353 ± 0.01
3	0.69 ± 0.03	24 ± 3	17 ± 2	0.309 ± 0.03
4	0.63 ± 0.02	16 ± 2	11 ± 2	0.386 ± 0.02
5	0.61 ± 0.02	18 ± 3	13 ± 2	0.3877 ± 0.02
20P + 0.1B				
1	0.801 ± 0.006	13.3 ± 0.4	9.2 ± 0.3	0.199 ± 0.006
2	0.943 ± 0.003	11.3 ± 0.2	7.8 ± 0.1	0.057 ± 0.003
3	0.949 ± 0.003	9.8 ± 0.2	6.8 ± 0.1	0.051 ± 0.003
4	0.919 ± 0.003	9.3 ± 0.2	6.4 ± 0.1	0.081 ± 0.003
5	0.722 ± 0.007	13.9 ± 0.6	9.6 ± 0.4	0.278 ± 0.007
20P + 1B				
1	0.856 ± 0.003	5.6 ± 0.1	3.9 ± 0.1	0.144 ± 0.003
2	0.763 ± 0.006	6.0 ± 0.4	4.1 ± 0.2	0.237 ± 0.006
3	0.92 ± 0.003	4.7 ± 0.1	3.24 ± 0.09	0.08 ± 0.003
4	1.048 ± 0.005	4.8 ± 0.2	3.3 ± 0.1	-0.048 ± 0.005
5	1.072 ± 0.004	6.9 ± 0.1	4.6 ± 0.1	-0.072 ± 0.004

D, therefore, the D value closer to the Stokes-Einstein relationship is the most reliable (Figure 5.5(b)).

Since there are several length scales present in the semi-dilute and concentrated PEG, PEG+B, and PEG+CMC, the application of the Stokes-Einstein equation to get an idea of the theoretical value of D can lead to improper estimates. Investigating the diffusion of gold nanoparticles in the semi-dilute regime of PEG solution using fluctuation correlation spectroscopy has shown that for the intermediate regime, the diffusion is faster than the Stokes-Einstein relationship and the diffusivity falls on a single curve depending on the concentration [52]. Therefore, the D values for PEG solutions are plotted as a function of concentration (c, in volume fraction) as shown in Figure 5.5(c) and it is observed that the mean D values follow Rouse scaling with $D \sim c^{-0.54}$ for c < 0.8, with decreasing D values on increasing the concentration [12]. An exponential decrease in the D values with polymer concentration is also observed in polyvinyl alcohol solutions in the intermediate regime [59].

The D values of only CMC solutions are independent of concentration, with

$D \sim c^0$, (Figure 5.5(d)). The D values for aqueous CMC solutions in the present case seem to be similar to the fast mode D-values obtained by dynamic light scattering experiments of CMC aqueous solutions, which also report additional slow and ultra-slow modes of diffusion. The fast mode of diffusion was independent of concentration, whereas the slow mode of diffusion was found to be strongly concentration dependent for CMC solutions [50]. Molecular dynamics simulations in polymer nanoparticle mixtures reveal that these fast and slow diffusing regions are dependent on the size of nanoparticles and the polymer entanglement mesh size [60]. Simulations have also revealed that the diffusion of nanoparticles in polymer nanocomposites is dependent on the presence of strong entropic and enthalpic interactions between the nanoparticle and polymer matrix which can form structures/networks in the system [61].

5.5 Micro-scale structuring in polymer solutions

To study micro-scale structures formed in polymer solutions and polymer nanocomposite solutions, static structure factor is calculated from the prebleach FRAP images. Phase contrast microscopy and scattering experiments are also performed to measure the structuring at different length scales.

5.5.1 Structure factor and 2D correlations from FRAP

To study the structures formed in the polymer nanocomposites, a 2-D correlation function is calculated from the prebleach fluorescence microscopy images of the solutions. This correlation function leads to the determination of the corresponding structure factor in Fourier space for the respective polymer nanocomposite solutions, i.e., PEG, PEG+CMC, and PEG+B solutions. The static and dynamic structure factors can be obtained by analyzing the microscopy images in Fourier space, it has been studied that the structure factors obtained from the aforementioned technique are similar to that obtained from dynamic light scattering experiments [62, 63]. However, structural studies using microscopy are advantageous over the traditional dynamic light scattering because a higher range of q values can be observed using microscopy, also the study of higher concentration solutions becomes easier and more reliable in

microscopy as compared to dynamic light scattering which experiences multiple scattering in highly concentrated solutions.

The 2D autocorrelation function is calculated from the confocal microscopy images obtained using fluorescent molecular probes in solutions of different concentrations of polymer and nanoparticles. According to the convolution theorem, the Fourier transform of a correlation function is obtained from the product of the Fourier transform of the image with the Fourier transform of its complex conjugate. Therefore, the 2D autocorrelation function is obtained by an inverse Fourier transform of the convolution of the 2D images obtained by a confocal microscope. In this method, time series microscopy images are analyzed in Fourier space, removing the requirement of any sophisticated instrumentation. Although it has been used to probe structural dynamics, it results in a very sensitive detection of the static structure factor. If the intensity at a point x' in a microscope image in real space with coordinates (x', y') is represented by I(x'), for the image of size N_x x N_y pixels (= 512 X 512 pixels for images in the present case) and magnification M, with l_p (= 0.414 μm/pixel in our experiments) the size of each pixel, then the structure factor, which is the Fourier space (Q space) representation of I(x') is given as $\tilde{I}(Q)$ (Equation 5.15) [62]

$$Q = \frac{2\pi M}{N_x N_y l_p} \tag{5.14}$$

$$\tilde{I}(Q) = \sum_p I(x'_p) e^{-i(Q.x'_p)} \tag{5.15}$$

In Equation 5.15, the summation is over all the pixels, p and x' or (x'_p, y'_p) is the coordinate of the p^{th} pixel. The above equation was used to calculate the structure factor from the confocal microscopy image of a sample (using the same setup as in FRAP experiments). Since imaging is done with a scanning confocal microscope, each image represents a thin section of the sample, so multiple scattering is negligible and the scattered fluorescence emission of the fluorescein is basically the scattered light captured, the transmitted illuminating beam is eliminated. The final static structure factor S(Q) is obtained by averaging the structure factor (Equation 5.15) obtained from 10 frames for each sample. To calculate the spatial correlations in two dimensions, a convolution is performed over the product of the image intensity matrix in Fourier space and its complex

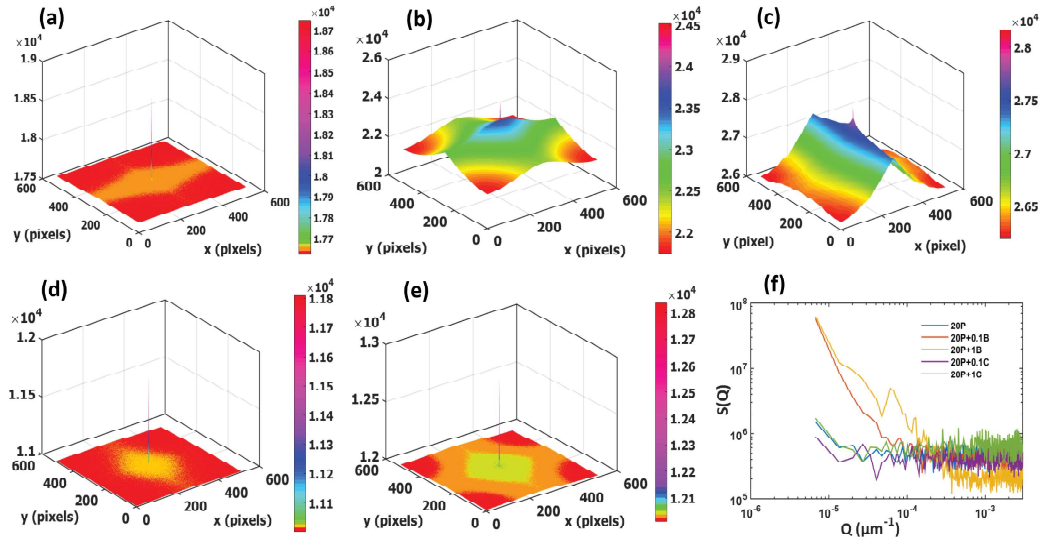

FIGURE 5.6: 2D spatial correlation function for (a) 20P; (b) 20P+0.1B (c) 20P+1B; (d) 20P+0.1C and (e) 20P+1C solutions. (f) Static structure factor S(Q) as a function of wave vector Q.

conjugate.

The 2D spatial autocorrelation functions for 20P, 20P+0.1B, 20P+1B, 20P+0.1C, and 20P+1C are shown in Figure 5.6(a)-(e) respectively. From Figure 5.6, it is observed that the correlation is highest when bentonite nanoparticles are present in the solution which is a result of the enhanced structural interactions in the PEG+B system. Also, the static structure factor, which is shown in Figure 5.6(f), shows a higher upturn at low q values for PEG + bentonite nanocomposites which indicate the presence of inhomogeneities due to the presence of bentonite aggregates. The deviation in structure factor is a signature of enthalpic interactions between the polymer and nanoparticles which has been observed in molecular dynamics simulations [61]. The results indicate the presence of aggregation bentonite nanoparticles due to depletion interaction which further needs to be studied. To affirm the presence of bentonite aggregates in the PEG matrix, phase contrast microscopy images are collected for varying concentrations of PEG in 1 wt.% bentonite.

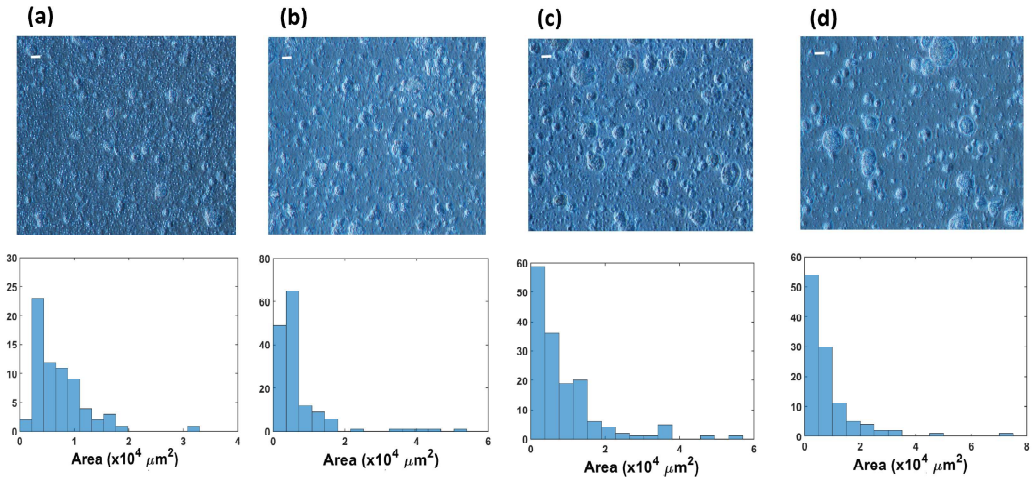

FIGURE 5.7: Phase contrast microscope images of bentonite structures with different concentrations of PEG (a) 2P; (b) 5P; (c) 10P and (d) 20P in the aqueous solution (scale bar = 10 μm) and the corresponding normalized histograms of the area of these structures.

5.5.2 Micro-scale structural analysis using phase contrast microscopy

Phase contrast microscopy is a technique that is used to produce high-contrast images of transparent or colorless specimens. It is a technique popularly used to study living cells, tissues, microorganisms, and subcellular bodies. In this technique, the light passing through a transparent sample is diffracted and phase shifted to convert into an amplitude difference which can be visualized in a microscope. Phase contrast microscopy was performed to study the bentonite aggregates in transparent PEG solutions. The phase contrast images were captured with a Nikon Eclipse TS100 microscope equipped with a Nikon 40x-0.60NA phase contrast ELWD objective with 300 msec. exposure time. The images were captured using a Nikon DS Fi2 camera with a resolution of 1μm/pixel. These images were then analyzed to determine the particle size distribution using imageJ software and custom-made programs in MATLAB.

Since the 2D correlation function obtained from FRAP shows the highest structuring and correlation in 1 wt.% bentonite, therefore 1 wt.% bentonite is fixed and four different concentrations: 2 wt.%, 5 wt.%, 10 wt.%, and 20 wt.% PEG were studied. The phase contrast images for all the concentrations of PEG

show the variable size of aggregation of bentonite nanoparticles as shown in Figure 5.7. It is observed that with increasing polymer concentration, the size of aggregates increases, and there is enhanced flocculation of the bentonite nanoparticles. The histograms show the probability of occurrence of larger-size bentonite aggregates as the PEG concentration is increasing from 2P to 20P as a function of the area of the aggregates. The average area of the bentonite aggregate size distributions are 7241 $\pm$ 621 μm^2 for 2P solution; 6820 $\pm$ 814 μm^2 for 5P solution; 8689 $\pm$ 854 μm^2 for 10P solution; and 8110 $\pm$ 1070 μm^2 for 20P solution. From the average area, the average size of bentonite aggregates are 96 $\pm$ 4 μm for 2P; 93 $\pm$ 5 μm for 5P; 105 $\pm$ 5 μm for 10P and 101 $\pm$ 6 μm for 20P solution.

The increase in the size of aggregates with increasing polymer concentration can be explained by the fact that with increasing polymer concentration, there is a higher amount of non-adsorbed polymer chains which can result in higher attractive entropic forces between the colloidal particles known as depletion interactions [64]. When two colloidal particles come closer than twice the radius of gyration of the polymer, then a net attractive force starts bringing the two particles together. The depletion force decreases the stability of the system by lowering the Coulomb barrier, thereby enhancing the clustering of nanoparticles [64]. The depletion force is active in a range equal to the radius of gyration of the polymer and is known as the depletion zone. The strength of the depletion force depends on the concentration and the size of the polymer. The presence of aggregates in the present study is an indication of the presence of depletion interactions which can possibly result in phase separation between the polymer and nanoparticle phases.

An approximate estimation of the depletion interaction potential is given in units of k_BT by

$$\frac{\phi_{Dep}}{k_BT} = -\frac{3b}{2R_g} \tag{5.16}$$

here, b is the radius of colloidal particles, R_g is the radius of gyration of the polymer and ϕ_{Dep} is the depletion interaction potential. In present scenario b $\approx$ 25 μm as calculated from the phase contrast images and R_g = 6.246 nm. The depletion potential varies from $\sim 3k_BT$ in 5P to $\sim 53k_BT$ in 50P as stated in Table 5.1 which indicates that the depletion interactions are strong enough to separate

the polymer and bentonite phases within the system at higher polymer concentrations. For 20P, the depletion interaction is $\sim 13 k_B T$ which tends to cause phase separation and can compete with the adsorption of PEG on clay surface which tends to form PEG-clay associated structures, leading to breakage of polymer-clay bridged networks. This can explain the heterogeneities observed in the FRAP experiments.

5.5.3 Small angle X-ray scattering (SAXS)

Small-angle X-ray scattering is a technique that is used to study the material structures and morphology at nanoscopic scales. It is an analytical technique that can probe the density differences within the samples, even a slight change in the electron density can be captured using SAXS. A major advantage of SAXS is that it can determine the structure of almost all types of materials from solids, liquids, and gases to colloids and gels. Here, we have performed SAXS experiments to determine the micro-scale structuring in PEG + bentonite solutions. We have used two different ranges to perform SAXS experiments at two different facilities to obtain different length scales of structuring.

1. Range 1 ($0.1\ nm^{-1}$ < q < $3\ nm^{-1}$) : These experiments were performed at Raja Ramanna Center for Advanced Technology (RRCAT), Indore. The small and wide angle X-ray scattering (SWAXS) beamline (BL-18) at INDUS-2 was used. A monochromatic X-ray beam was obtained from a 1.5 Tesla bending magnet-based synchrotron X-ray source. The scattered X-rays were detected using a 2-Dimension online image plate. The exposure time was set to 180 seconds for all the samples.

2. Range 2 ($0.01\ nm^{-1}$ < q < $1\ nm^{-1}$) : These measurements were conducted at Sophisticated Analytical Instrument Facility (SAIF), IIT, Bombay. The experiments were performed on Xesus 2.0 apparatus (from Xenocs SAS). A Cu k_α radiation (generated from GeniX3D Cu 30Watts Cu tube with 50KV and 0.6mA current) of wavelength 1.54 Åwas incident on the sample. The X-rays scattered from the sample were detected with Eiger R 1M, a 2D high-resolution hybrid pixel photon counting detector with 75 μm pixel size. The exposure time was 30 minutes for all the samples.

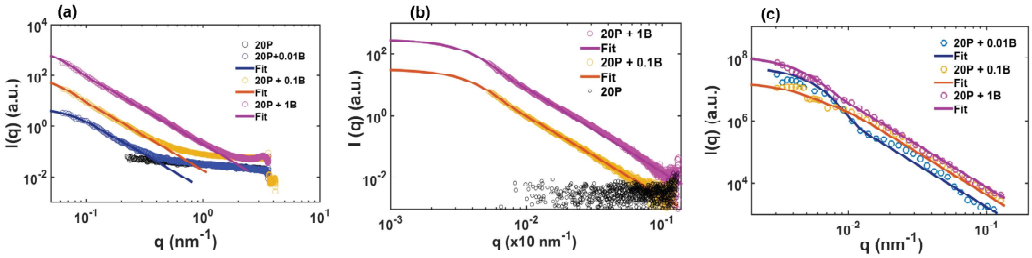

FIGURE 5.8: SAXS intensity I(q) as a function of the scattering wave vector q (a) for q varying between 0.1 nm^{-1} to 3 nm^{-1} and (b) for q varying between 0.01 to 1 nm^{-1} for PEG + bentonite solutions. (c) MSANS intensity I(q) as a function of the scattering wave vector q for PEG + bentonite solutions. The line curves are fits to Equation 5.18.

TABLE 5.4: Aggregate size obtained from fitting hierarchical model (Equation 5.18) to scattering intensity obtained in SAXS and MSANS. SAXS 1 is the SAXS experiments for the range given in Figure 5.8(a) (range 1) and SAXS 2 is the SAXS experiments for the range given in Figure 5.8(b) (range 2). The average aggregate size obtained from phase contrast microscopy for different concentrations of polymer in 1 wt.% bentonite solutions.

Sample	a (constant)	R_{ss} (nm)	c (constant)	Adj. r^2
SAXS 1				
20P + 0.01B	0.00341 ± 0.0001	21.4 ± 0.8	2.7 ± 0.3	0.99
20P + 0.1B	0.01803 ± 0.0001	33.1 ± 0.7	120 ± 8	0.99
20P + 1B	0.1922 ± 0.0005	34.4 ± 0.2	1518 ± 40	0.99
SAXS 2				
20P + 0.1B	$4.05x10^{-6} \pm 0.8x10^{-8}$	46 ± 0.2	35.6 ± 0.5	0.99
20P + 1B	$3.11x10^{-5} \pm 0.6x10^{-7}$	47.3 ± 0.3	300 ± 5	0.99
MSANS				
20P + 0.01B	3.4 ± 0.4	360 ± 18	$5.510^{7} \pm 1.3x10^{7}$	0.99
20P + 0.1B	8 ± 2	385 ± 172	$1.7x10^{7} \pm 1.1x10^{7}$	0.98
20P + 1B	14 ± 2	410 ± 56	$1.1x10^{8} \pm 0.4x10^{8}$	0.99
Phase contrast microscopy				
Sample	average size (d = 2r) (μm)			
2P + 1B	96 ± 4			
5P + 1B	93 ± 5			
10P + 1B	105 ± 5			
20P + 1B	101 ± 4			

The SAXS experiments for 20P shows negligible scattering intensity (Figure 5.8(a)) whereas, on addition of bentonite nanoparticles, the scattering intensity increases. On adding 0.01 wt.% bentonite, the scattering intensity is very small but the addition of 0.1 wt.% and 1 wt.% bentonite to 20P increases the scattering intensity to 100 times. The increase in scattering intensity is a result of the hierarchical structures present in the solutions with higher bentonite concentrations. Nanoparticles have been observed to form hierarchical structures in polymer matrix spreading over several length scales. Most often, these structures have fractal dimensions. The unified Guinier and power law model developed by Beaucage et. al [65, 66, 67]. is a successful model to estimate the hierarchical structures which can be obtained from all the scattering techniques which is given by:

$$\begin{aligned} I(q) = & [A\exp(-q^2R_{gg}^2/3)q^{-4} + B\exp(-q^2R_{gg}^2/3) \\ & + C\exp(-q^2R_{gg}^2/3) \times [\frac{erf(\frac{qR_{ss}}{\sqrt{6}})^3}{q}]^{2.3} \\ & + D\exp(-q^2R_{gg}^2/3) + E[\frac{erf(\frac{qR_{ss}}{\sqrt{6}})^3}{q}]^{6-D_s}] \end{aligned} \tag{5.17}$$

Estimation of several length scales in the hierarchical structuring requires wide angle, small angle as well as ultra-small angle scattering data spanning several decades in the scattering wave vector, q. Considering the limited q range of the SAXS data in Figure 5.8(a), one structural level of hierarchical structuring could be estimated by limiting the hierarchical fractal model (Equation 5.17) for one structural level of the cluster which can be given by the following equation:

$$I(q) = a[\frac{\{erf(\frac{qR_{ss}}{\sqrt{6}})^3\}}{q}]^n + c[exp(\frac{-q^2R_{ss}^2}{3})] \tag{5.18}$$

Since the hierarchical structures have several length scales associated with them, the SAXS experiments are extended to a lower q range, the scattering intensity observed in the low q range is given in Figure 5.8(b). In this range also, the 20P shows negligible scattering and the scattering intensity is higher on adding 0.1 wt.% and 1 wt.% bentonite to 20P. The scattering experiments are also extended to further study the structural hierarchy using MSANS experiments.

5.5.4 Medium resolution small angle neutron scattering (MSANS)

Small angle neutron scattering (SANS) is also a technique used to study the material structures and morphology but at the mesoscale, i.e., for the structures ranging from nanoscale to microscale. It is a powerful technique to study the morphology of complex macrostructures like polymers, biomolecules, micelles, and various magnetic systems. Since neutrons are penetrating in most materials, SANS becomes an excellent non-destructive technique to study the morphology of materials. SANS experiences scattering from magnetic moments which is a strong scattering and it is also sensitive to light elements which makes it advantageous over SAXS. The MSANS experiments are performed to study the micro-structures formed in PEG + bentonite nanocomposites. The MSANS experiments were performed at the Dhruva reactor facility at Bhabha Atomic Research Center (BARC), Mumbai, India on a double crystal-based MSANS setup. A neutron beam of wavelength 3.12 Åwas incident on the sample through the beam port Guide G1 and the monochromator Si(111). The sample was placed between Si single crystals and the instrument was working on a non-dispersive (-1,1) setting of (111) reflections of Si single crystals. The experiments were performed for the q ranging from 0.001 nm^{-1} to 0.1 nm^{-1}. The scattered beam was detected using a BF_3 counter.

The MSANS scattering intensity for all 3 concentrations of PEG + B solutions show similar scattering intensities (Figure 5.8(c)). On fitting the scattering intensities to the hierarchical model given by Equation 5.18, three different length scales are obtained. The results after fitting Equation 5.18 to all the scattering ranges observed are given in Table 5.4. From the values of R_{ss} obtained from fitting, we can conclude that the aggregation of bentonite nanoparticles in PEG + B solutions have several length scales and we are able to successfully determine three length scales from the scattering as well as phase contrast microscopy experiments. The structure factor calculated from the pre-bleach confocal microscopy images also demonstrates the presence of aggregates which is sensitive to bentonite concentration.

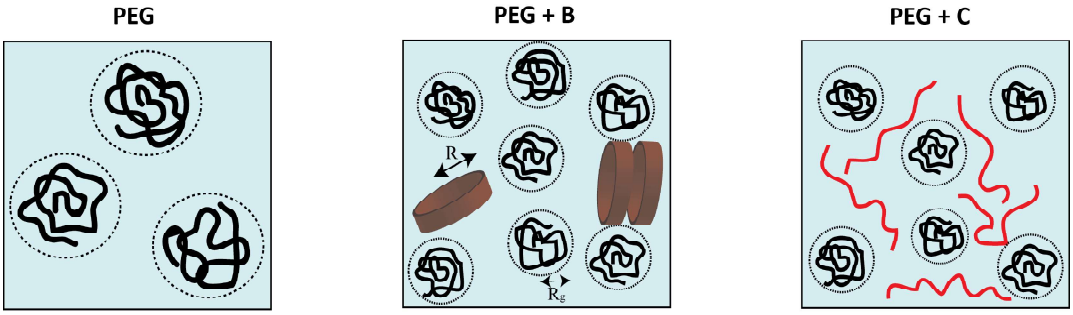

FIGURE 5.9: Schematic representation of PEG solution without nanoparticles on the left followed by incorporating bentonite nanoparticles in PEG solution (in the middle) and on adding CMC nanofibers in PEG (on extreme right). The bentonite nanoparticles are disc-like structures that aggregate due to depletion interactions. The R_g is the radius of gyration of PEG and R is the length scale of bentonite aggregates obtained from scattering experiments.

5.6 Summary

The incorporation of nanoparticles or fillers into a polymer matrix has played an important role in altering the mechanical properties of the resultant nanocomposite material. In the present study, we have shown the effect of dispersing two types of fillers: bentonite nanoparticles and CMC nanofibers into PEG matrix and studied their effect on the micro-scale mechanical properties using microscopic techniques like FRAP and scattering techniques. From the diffusion analysis using FRAP, micro-scale heterogeneities are observed in bentonite solutions whereas, in CMC solutions, immobile fractions are present. The scattering experiments complemented the results obtained with FRAP resulting in the presence of depletion interaction-induced aggregation in PEG + bentonite solutions. This affirms that FRAP is a sensitive and efficient tool not only to study the diffusion dynamics of the system but also the structural heterogeneities present in the system. The effect of aggregation is also reflected in the D values calculated using FRAP which underlines the fact that the aggregation of clay particles affects the mechanical properties of the nanocomposite material, therefore clay particles can effectively be used as fillers to tune the mechanical properties of any material. The study of aggregation also ascertains that the micro-scale inhomogeneities present in the material can affect the microscopic mechanical properties which can in turn affect the macroscopic

mechanical response of the material. Therefore, for better applicability of a nanocomposite, it is necessary to study the micro-level inhomogeneities and heterogeneities present in the nanocomposite material.

Refernces

[1] Iriny Ekladious, Yolonda L Colson, and Mark W Grinstaff. Polymer–drug conjugate therapeutics: advances, insights and prospects. *Nature reviews Drug discovery*, 18(4):273–294, 2019.

[2] Melis Goktas, Goksu Cinar, Ilghar Orujalipoor, Semra Ide, Ayse B Tekinay, and Mustafa O Guler. Self-assembled peptide amphiphile nanofibers and peg composite hydrogels as tunable ecm mimetic microenvironment. *Biomacromolecules*, 16(4):1247–1258, 2015.

[3] Chien-Chi Lin and Kristi S Anseth. Peg hydrogels for the controlled release of biomolecules in regenerative medicine. *Pharmaceutical research*, 26(3):631–643, 2009.

[4] Sudipta Senapati, Arun Kumar Mahanta, Sunil Kumar, and Pralay Maiti. Controlled drug delivery vehicles for cancer treatment and their performance. *Signal transduction and targeted therapy*, 3(1):1–19, 2018.

[5] Shangjing Xin, David Chimene, Jay E Garza, Akhilesh K Gaharwar, and Daniel L Alge. Clickable peg hydrogel microspheres as building blocks for 3d bioprinting. *Biomaterials science*, 7(3):1179–1187, 2019.

[6] Nádia SV Capanema, Alexandra AP Mansur, Anderson C de Jesus, Sandhra M Carvalho, Luiz C de Oliveira, and Herman S Mansur. Superabsorbent crosslinked carboxymethyl cellulose-peg hydrogels for potential wound dressing applications. *International journal of biological macromolecules*, 106:1218–1234, 2018.

[7] Chien-Wen Chang, Ariane Van Spreeuwel, Chao Zhang, and Shyni Varghese. Peg/clay nanocomposite hydrogel: a mechanically robust tissue engineering scaffold. *Soft Matter*, 6(20):5157–5164, 2010.

[8] A Inamuddin and Ali Mohammad. *Applications of nanocomposite materials in drug delivery*. Elsevier, 2018.

[9] Fangfang Song, Xiaoqiong Li, Qun Wang, Liqiong Liao, and Chao Zhang. Nanocomposite hydrogels and their applications in drug delivery and tissue engineering. *Journal of biomedical nanotechnology*, 11(1):40–52, 2015.

[10] S Lüsse and K Arnold. The interaction of poly (ethylene glycol) with water studied by 1h and 2h nmr relaxation time measurements. *Macromolecules*, 29(12):4251–4257, 1996.

[11] Adrian S Muresan, Johan LA Dubbeldam, Holger Kautz, Michael Monkenbusch, Rint P Sijbesma, Paul van der Schoot, and Wim H de Jeu. Dynamic heterogeneity in hydrogen-bonded polymers. *Physical Review E*, 74(3):031804, 2006.

[12] Zhijie Zhang, Chongwen Huang, RA Weiss, and Quan Chen. Association energy in strongly associative polymers. *Journal of Rheology*, 61(6):1199–1207, 2017.

[13] Ronald G Larson. *The structure and rheology of complex fluids*, volume 150. Oxford university press New York, 1999.

[14] J Brassinne, A Cadix, J Wilson, and Evelyne Van Ruymbeke. Dissociating sticker dynamics from chain relaxation in supramolecular polymer networks—the importance of free partner! *Journal of Rheology*, 61(6):1123–1134, 2017.

[15] Milad Golkaram and Katja Loos. A critical approach to polymer dynamics in supramolecular polymers. *Macromolecules*, 52(24):9427–9444, 2019.

[16] Ludwik Leibler, Michael Rubinstein, and Ralph H Colby. Dynamics of reversible networks. *Macromolecules*, 24(16):4701–4707, 1991.

[17] Michael Rubinstein and Alexander N Semenov. Dynamics of entangled solutions of associating polymers. *Macromolecules*, 34(4):1058–1068, 2001.

[18] Zhijie Zhang, Quan Chen, and Ralph H Colby. Dynamics of associative polymers. *Soft Matter*, 14(16):2961–2977, 2018.

[19] Dipesh Amin, Alexei E Likhtman, and Zuowei Wang. Dynamics in supramolecular polymer networks formed by associating telechelic chains. *Macromolecules*, 49(19):7510–7524, 2016.

[20] Dipesh Amin and Zuowei Wang. Nonlinear rheology and dynamics of supramolecular polymer networks formed by associative telechelic chains under shear and extensional flows. *Journal of Rheology*, 64(3):581–600, 2020.

[21] BJ Gold, CH Hovelmann, N Luhmann, NK Szkely, W Pyckhout-Hintzen, A Wischnewski, and D Richter. Importance of compact random walks for the rheology of transient networks. *ACS Macro Letters*, 6(2):73–77, 2017.

[22] Mithil Kamble, Aniruddha Singh Lakhnot, Nikhil Koratkar, and Catalin R Picu. Heterogeneity-induced mesoscale toughening in polymer nanocomposites. *Materialia*, 11:100673, 2020.

[23] Hossein A Baghdadi, Justin Parrella, and Surita R Bhatia. Long-term aging effects on the rheology of neat laponite and laponite-peo dispersions. *Rheologica Acta*, 47(3):349–357, 2008.

[24] Hossein A Baghdadi, Heidi Sardinha, and Surita R Bhatia. Rheology and gelation kinetics in laponite dispersions containing poly (ethylene oxide). *Journal of Polymer Science Part B: Polymer Physics*, 43(2):233–240, 2005.

[25] Ralph H Colby. Structure and linear viscoelasticity of flexible polymer solutions: comparison of polyelectrolyte and neutral polymer solutions. *Rheologica acta*, 49(5):425–442, 2010.

[26] Vikram K Daga and Norman J Wagner. Linear viscoelastic master curves of neat and laponite-filled poly (ethylene oxide)–water solutions. *Rheologica acta*, 45(6):813–824, 2006.

[27] John R de Bruyn, Frédéric Pignon, Emir Tsabet, and Albert Magnin. Micron-scale origin of the shear-induced structure in laponite–poly (ethylene oxide) dispersions. *Rheologica Acta*, 47(1):63–73, 2008.

[28] Gudrun Schmidt, Alan I Nakatani, and Charles C Han. Rheology and flow-birefringence from viscoelastic polymer-clay solutions. *Rheologica Acta*, 41(1):45–54, 2002.

[29] Daniel Bonn, Morton M Denn, Ludovic Berthier, Thibaut Divoux, and Sébastien Manneville. Yield stress materials in soft condensed matter. *Reviews of Modern Physics*, 89(3):035005, 2017.

[30] Thibaut Divoux, David Tamarii, Catherine Barentin, and Sébastien Manneville. Transient shear banding in a simple yield stress fluid. *Physical review letters*, 104(20):208301, 2010.

[31] Rahul Pandey and Jacinta C Conrad. Gelation in mixtures of polymers and bidisperse colloids. *Physical Review E*, 93(1):012610, 2016.

[32] Marco Laurati, George Petekidis, Nick Koumakis, Fred Cardinaux, Andrew B Schofield, Joseph M Brader, Matthias Fuchs, and Stefan Ulrich Egelhaaf. Structure, dynamics, and rheology of colloid-polymer mixtures: From liquids to gels. *The Journal of chemical physics*, 130(13):134907, 2009.

[33] Makiko Takeda, Takuro Matsunaga, Toshihiko Nishida, Hitoshi Endo, Tsutomu Takahashi, and Mitsuhiro Shibayama. Rheo-sans studies on shear thickening in clay- poly (ethylene oxide) mixed solutions. *Macromolecules*, 43(18):7793–7799, 2010.

[34] AR Denton. Nonlinear screening and effective electrostatic interactions in charge-stabilized colloidal suspensions. *Physical Review E*, 70(3):031404, 2004.

[35] Thomas Eckert and Eckhard Bartsch. Re-entrant glass transition in a colloid-polymer mixture with depletion attractions. *Physical review letters*, 89(12):125701, 2002.

[36] J Opdam, MPM Schelling, and R Tuinier. Phase behavior of binary hard-sphere mixtures: Free volume theory including reservoir hard-core interactions. *The Journal of Chemical Physics*, 154(7):074902, 2021.

[37] Álvaro González García and Remco Tuinier. Tuning the phase diagram of colloid-polymer mixtures via yukawa interactions. *Physical Review E*, 94(6):062607, 2016.

[38] Nayoung Park, Vikram Rathee, Daniel L Blair, and Jacinta C Conrad. Contact networks enhance shear thickening in attractive colloid-polymer mixtures. *Physical Review Letters*, 122(22):228003, 2019.

[39] José Ruiz-Franco, Fabrizio Camerin, Nicoletta Gnan, and Emanuela Zaccarelli. Tuning the rheological behavior of colloidal gels through competing interactions. *Physical Review Materials*, 4(4):045601, 2020.

[40] V Trappe and DA Weitz. Scaling of the viscoelasticity of weakly attractive particles. *Physical review letters*, 85(2):449, 2000.

[41] Niklas Lorén, Joel Hagman, Jenny K Jonasson, Hendrik Deschout, Diana Bernin, Francesca Cella-Zanacchi, Alberto Diaspro, James G McNally, Marcel Ameloot, Nick Smisdom, et al. Fluorescence recovery after photobleaching in material and life sciences: putting theory into practice. *Quarterly reviews of biophysics*, 48(3):323–387, 2015.

[42] Aref Abbasi Moud. Fluorescence recovery after photobleaching in colloidal science: Introduction and application. *ACS Biomaterials Science & Engineering*, 8(3):1028–1048, 2022.

[43] Lan Yu, Yunze Lei, Ying Ma, Min Liu, Juanjuan Zheng, Dan Dan, and Peng Gao. A comprehensive review of fluorescence correlation spectroscopy. *Frontiers in physics*, 9:644450, 2021.

[44] Radek Macháň, Yong Hwee Foo, and Thorsten Wohland. On the equivalence of fcs and frap: simultaneous lipid membrane measurements. *Biophysical journal*, 111(1):152–161, 2016.

[45] Minchul Kang, Charles A Day, Anne K Kenworthy, and Emmanuele DiBenedetto. Simplified equation to extract diffusion coefficients from confocal frap data. *Traffic*, 13(12):1589–1600, 2012.

[46] Minchul Kang, Manuel Andreani, and Anne K Kenworthy. Validation of normalizations, scaling, and photofading corrections for frap data analysis. *PLoS One*, 10(5):e0127966, 2015.

[47] Jun Wu, Nandini Shekhar, Pushkar P Lele, and Tanmay P Lele. Frap analysis: accounting for bleaching during image capture. 2012.

[48] Daniel Axelrod, DE Koppel, J Schlessinger, Elliot Elson, and Watt W Webb. Mobility measurement by analysis of fluorescence photobleaching recovery kinetics. *Biophysical journal*, 16(9):1055–1069, 1976.

[49] Daniel Blumenthal, Leo Goldstien, Michael Edidin, and Levi A Gheber. Universal approach to frap analysis of arbitrary bleaching patterns. *Scientific reports*, 5(1):1–9, 2015.

[50] Juliette S Behra, Johan Mattsson, Olivier J Cayre, Eric SJ Robles, Haiqiu Tang, and Timothy N Hunter. Characterization of sodium carboxymethyl cellulose aqueous solutions to support complex product formulation: A rheology and light scattering study. *ACS Applied Polymer Materials*, 1(3):344–358, 2019.

[51] Tao Chen, Hu-Jun Qian, and Zhong-Yuan Lu. Diffusion dynamics of nanoparticle and its coupling with polymers in polymer nanocomposites. *Chemical Physics Letters*, 687:96–100, 2017.

[52] Indermeet Kohli and Ashis Mukhopadhyay. Diffusion of nanoparticles in semidilute polymer solutions: Effect of different length scales. *Macromolecules*, 45(15):6143–6149, 2012.

[53] Sanat K Kumar, Brian C Benicewicz, Richard A Vaia, and Karen I Winey. 50th anniversary perspective: are polymer nanocomposites practical for applications? *Macromolecules*, 50(3):714–731, 2017.

[54] Kirtland L Linegar, Adedao E Adeniran, Andrei F Kostko, and Mikhail A Anisimov. Hydrodynamic radius of polyethylene glycol in solution obtained by dynamic light scattering. *Colloid journal*, 72(2):279–281, 2010.

[55] Yuri Chenyakin, Dagny A Ullmann, Erin Evoy, Lindsay Renbaum-Wolff, Saeid Kamal, and Allan K Bertram. Diffusion coefficients of organic molecules in sucrose–water solutions and comparison with stokes–einstein predictions. *Atmospheric Chemistry and Physics*, 17(3):2423–2435, 2017.

[56] A Sorrentino, M Tortora, and V Vittoria. Diffusion behavior in polymer–clay nanocomposites. *Journal of Polymer Science Part B: Polymer Physics*, 44(2):265–274, 2006.

[57] Carlos G Lopez, Sarah E Rogers, Ralph H Colby, Peter Graham, and Joao T Cabral. Structure of sodium carboxymethyl cellulose aqueous solutions: A sans and rheology study. *Journal of Polymer Science Part B: Polymer Physics*, 53(7):492–501, 2015.

[58] Ramanand Singh Yadav, Chintu Das, and Rajarshi Chakrabarti. Dynamics of a spherical self-propelled tracer in a polymeric medium: interplay of self-propulsion, stickiness, and crowding. *Soft Matter*, 2023.

[59] Ariel Michelman-Ribeiro, Ferenc Horkay, Ralph Nossal, and Hacene Boukari. Probe diffusion in aqueous poly (vinyl alcohol) solutions studied by fluorescence correlation spectroscopy. *Biomacromolecules*, 8(5):1595–1600, 2007.

[60] Jagannathan T Kalathi, Umi Yamamoto, Kenneth S Schweizer, Gary S Grest, and Sanat K Kumar. Nanoparticle diffusion in polymer nanocomposites. *Physical review letters*, 112(10):108301, 2014.

[61] Monojoy Goswami and Bobby G Sumpter. Anomalous chain diffusion in polymer nanocomposites for varying polymer-filler interaction strengths. *Physical Review E*, 81(4):041801, 2010.

[62] Stefano Aime and Luca Cipelletti. Probing shear-induced rearrangements in fourier space. ii. differential dynamic microscopy. *Soft Matter*, 15(2):213–226, 2019.

[63] Roberto Cerbino and Veronique Trappe. Differential dynamic microscopy: probing wave vector dependent dynamics with a microscope. *Physical review letters*, 100(18):188102, 2008.

[64] Christoph Gögelein, Gerhard Nägele, Johan Buitenhuis, Remco Tuinier, and Jan KG Dhont. Polymer depletion-driven cluster aggregation and initial phase separation in charged nanosized colloids. *The Journal of chemical physics*, 130(20):204905, 2009.

[65] Gregory Beaucage and Dale W Schaefer. Structural studies of complex systems using small-angle scattering: a unified guinier/power-law approach. *Journal of non-crystalline solids*, 172:797–805, 1994.

[66] G Beaucage. Approximations leading to a unified exponential/power-law approach to small-angle scattering. *Journal of Applied Crystallography*, 28(6):717–728, 1995.

[67] Mikihito Takenaka. Analysis of structures of rubber-filler systems with combined scattering methods. *Polymer journal*, 45(1):10–19, 2013.